Fracture Toughness of Li_xSi Alloys in Lithium Ion Battery

Hui Yang[1, 2*], Jianmin Qu[2*]

[1]State Key Laboratory of Material Processing and Die & Mould Technology, Department of Mechanics, Huazhong University of Science and Technology, Wuhan, Hubei 430074, China

[2]Department of Mechanical Engineering, Tuft University, Medford, MA 02155, USA

*Corresponding author: huiyang2017@hust.edu.cn; jianmin.qu@tufts.edu ;

Abstract:

Fundamental understanding of the fracture toughness of the Li_xSi alloys is crucial for designing of Si based high-capacity and failure-resistant electrodes. In this study, molecular dynamics simulation informed continuum chemo-mechanical modelings with conservation integrals were conducted to derive fracture toughness of Li_xSi alloys. Our modeling results show reasonable agreement with available experimental data, revealing that the fracture toughness of Li_xSi alloys with low lithium concentration does not vary significantly with lithium concentration. In addition, we demonstrated that, if lithium redistribution caused by the stress gradient around crack tip needs to be considered, an appropriate chemo-mechanical path-independent J-integral should be used as the classic Rices J -integral is path-dependent. The obtained fracture toughness of the Li_xSi alloys here

provides guidance for the rational design of Si based electrodes, and the presented approach also sheds light for the evaluation of the fracture toughness of other energy materials at different charging/discharging levels.

Keywords:

Lithium ion battery; Li_xSi alloy; molecular dynamics simulation; chemo-mechanical model; fracture toughness; lithium redistribution

1. Introduction

Lithium (Li) ion batteries (LIBs), due to their high energy density, have been dominantly used as power sources in portable electronics.[1-4] However, the relative low capacity of currently commercialized LIBs has seriously hindered their extensive application in some emerging applications, such as electric vehicles and large energy grid.[5-7] It is well-known that silicon (Si) stands as one of the most promising anode materials owing to its highest theoretical capacity (4200 mAh/g).[8-10] Nevertheless, Li insertion/extraction during charging/discharging cyclings will inherently induce huge volumetric change and stress inside the Si anode, leading to fracture, pulverization, electrical disconnectivity, and ultimately capacity loss.[11-18] Therefore, a fundamental understanding of the degradation mechanisms in the Si anode during lithiation/delithiation cyclings, especially the damage initiation and propagation, is crucial for the rational design

of next-generation failure-resistant Si based electrodes.

Recent experimental studies evidenced that crystalline Si (*c*-Si) undergoes ~300% volumetric change during lithiation/delithiation cyclings, leading to the fracture of Si nano-particles even in the first lithiation cycle when the particle size is larger than ~150 nm.[11, 15-16, 19] For amorphous Si (*a*-Si), the volumetric change is ~280%.[20-21] However, the critical fracture size of *a*-Si particles can increase to ~870 nm.[20] In order to investigate the fracture behavior of lithiated Si, Pharr *et al*. estimated the fracture energy of lithiated Si thin film by measuring the curvature changes of the film at different lithiation and delithiation stages, concluding that the fracture energy of lithiated Si is almost independent of Li concentration as the obtained fracture toughness is $8.5 \pm 4.3\ \mathrm{J/m^2}$ at low Li concentration (~$Li_{0.7}Si$) and has the bounds of $5.4 \pm 2.2\ \mathrm{J/m^2}$ to $6.9 \pm 1.9\ \mathrm{J/m^2}$ at high Li concentration (~$Li_{2.8}Si$).[22] However, the nanoindentation based measurements conducted by Wang *et al*. revealed a highly Li concentration dependent fracture behavior of lithiated Si, namely, with the increment of Li concentration, the fracture toughness first decreases from $2.85 \pm 0.15\ \mathrm{J/m^2}$ for unlithiated *a*-Si to a minimum value at $Li_{0.31}Si$, and then increases substantially, reaching to $8.54 \pm 0.72\ \mathrm{J/m^2}$ for $Li_{1.09}Si$, which indicates a brittle-to-ductile transition of fracture with the increase of Li concentration in Si.[23] In consideration of the discrepancy between these two experimental studies, it is worthwhile to further investigate of the fracture toughness of Li_xSi as it ultimately dictates the cyclability of Si based electrodes.

Previous works have demonstrated that molecular dynamics (MD) simulation can be adopted as an appropriate method to computationally assess the fracture properties of

materials.[24-28] For instance, a perfect match was found between the MD simulation results and experimental data for *c*-Si structures, indicating that MD simulation is capable to calculate the fracture toughness.[24-26] However, as the lithiated Li_xSi can undergo relatively large plastic deformation before fracture failure compared with unlithiated Si, attentions should be paid to the large scale yielding around crack tip when calculating fracture toughness.[29-32] Therefore, in this study, a MD simulation informed continuum chemo-mechanical model is presented for the calculation of fracture toughness of Li_xSi alloys. In particular, MD simulations are conducted for the material properties of Li_xSi alloys (i.e., Young's modulus, Poisson's ratio, and yield stress) and the critical fracture strain under which the crack in the pre-cracked specimen starts to propagate. Based on the obtained material properties and critical fracture strain, a continuum chemo-mechanical model is used to calculate the stress distribution in the same cracked specimen under the corresponding critical strain loading. With the stress distribution information, J-integral is directly calculated for the fracture toughness of Li_xSi alloys.

2. Methodology

2.1. MD simulation

In our MD simulation, the newly developed second nearest-neighbor modified embedded atom method interatomic potential (2NN MEAM) of Li-Si alloy is adopted to account for the interactions among Li and Si atoms.[33-34] This 2NN-MEAM interatomic potential has been adequately demonstrated to provide the primary properties and lattice

structures of both crystalline and amorphous Li_xSi alloy successfully.[33] Based on this potential, MD simulations are conducted for the material properties of Li_xSi alloys and the critical fracture strain under which the crack in the pre-cracked specimen starts to propagate.

The atomic structures of different Li_xSi alloys are created by melting-quenching method.[35] First, large enough pure *c*-Si block is generated by using LAMMPS MD simulator. Second, according to the ratio x between the number of Li and Si atoms of different Li_xSi alloys, Li atoms are randomly inserted into the Si block for the corresponding compositions. Then, with periodic boundary conditions (PBCs) prescribed in all three dimensions of the simulation cell and the time step set to be 1 fs, the temperature of the Li_xSi block is increased from 0 K to 2500 K during the first 100 ps, and maintained there for another 400 ps, and afterward decreased to 10 K with quenching rate ~5.0 K/ps during the following 500 ps. Finally, the obtained fully amorphized Li_xSi block is relaxed for another 500 ps using NPT ensemble.

To understand the mechanical behaviors of Li_xSi alloys, MD simulations at 10 K are conducted to obtain the uniaxial tensile stress-strain relationships. Columns (30 × 30 × 80 Å in x, y, and z directions) are cut from the fully relaxed Li_xSi blocks. Tensile simulations with NPT ensemble are carried out by applying a constant strain rate (5×10^7 1/s) along the axial direction (z direction) of the columns. In addition, PBCs are prescribed in all three directions of the simulation box and the pressure on the other two non-loading directions is relaxed to zero to ensure the uniaxial tension of the columns. Based on the obtained stress-strain curves, the mechanical properties of Li_xSi alloys, such

as Young's modulus and yield stress, are estimated.

For the study of the fracture behaviors of Li_xSi alloys, simulation cells with the size of 500 × 350 × 15 Å in x, y, and z directions are cut from the fully relaxed Li_xSi blocks. PBCs are applied in both y and z directions. An edge crack with $a_0 = 90$ Å initial length and 4 Å width in x-y plane is created in the middle of the cell along x direction, as illustrated in Figure 1(a). After fully relaxed, the cell is stretched in y direction by changing the length of simulation box with a constant strain rate $5\times10^7\,1/s$. All the MD simulations are conducted at 10 K in LAMMPS with 1 fs time step. The strain at the critical moment that the crack starts to propagate is recorded for the next step chemo-mechanical calculations.

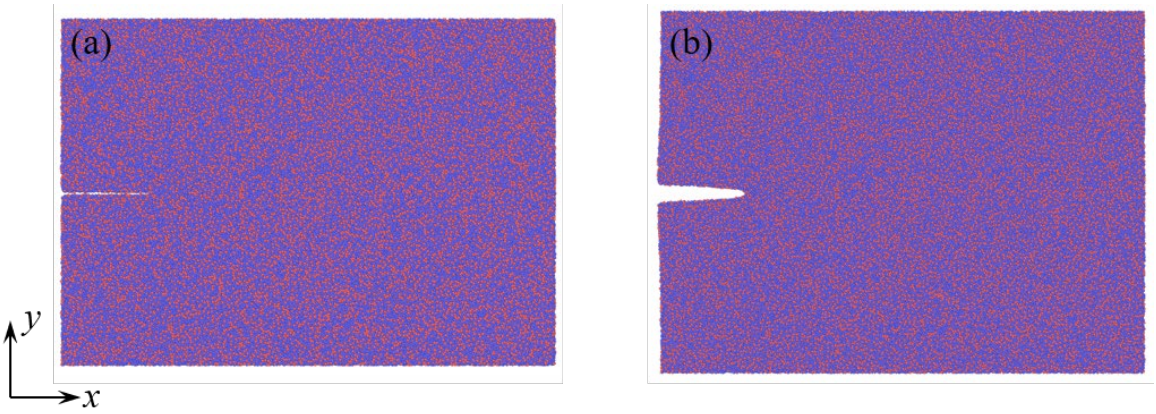

Figure 1. A typical Li_xSi alloy cell for MD simulation with a pre-existed edge crack. (a) Initially, the size of the simulation cell is about 500, 350, and 15 Å in *x*, *y*, and *z* dimensions, respectively. Initially, the crack is about 90 Å in length and 4 Å in width. (b) Configuration of the simulation cell at the critical moment that the crack starts to propagate.

2.2. Chemo-mechanical simulation

The previously developed finite strain chemo-mechanical model is adopted in this study.[18, 32, 36] In this model, the concurrent chemical reaction and diffusion processes are simulated in a unified manner by a non-linear diffusion model, despite the difference in interfacial reaction and bulk diffusion. Therefore, the classical diffusion equation is used to describe Li transport in the Si:

$$\frac{\partial c}{\partial t} = \nabla \cdot \mathbf{J}_{\mathrm{F}}, \qquad \mathbf{J}_{\mathrm{F}} = -D\nabla\mu, \tag{1}$$

where, c is the Li concentration, D is the diffusion constant, $\mathbf{J}_{\mathrm{F}}$ is the Li flux that related to the chemical potential of Li, μ, in Si defined as follows:[37]

$$\mu = \mu_0 + R_g T \log\frac{c}{c_{\max} - c} - V_m \eta \sigma_{kk}. \tag{2}$$

The $\mu_0 + R_g T \log\frac{c}{c_{\max} - c}$ and $V_m \eta \sigma_{kk}$ are the stress-independent and stress-dependent parts of the chemical potential, respectively. μ_0 is a constant representing the chemical potential at a standard state, R_g is the gas constant, $c_{\max}$ is the concentration corresponding to the saturation state, V_m is the molar volume, η is the coefficient of compositional expansion, and σ_{kk} is the trace of stress tensor. For the mechanics part of the model, the finite-strain elasto-plastic framework is used, in which the total stretch rate tensor $\mathbf{d}$ is decomposed into three additive parts:

$$\mathbf{d} = \mathbf{d}^e + \mathbf{d}^p + \mathbf{d}^c, \tag{3}$$

where, $\mathbf{d}^e$, $\mathbf{d}^p$, and $\mathbf{d}^c$ are the elastic, plastic, and chemical stretch rates, respectively. With the same-size edge-cracked Li_xSi samples as used in above MD simulation, the following equilibrium equation:

$$\nabla \cdot \boldsymbol{\sigma} = 0 \tag{4}$$

is solved with corresponding boundary conditions. All the material properties obtained from the above MD simulations, such as Young's modulus, Poisson's ratio, and yield stress, are adopted as inputs for the modeling. Using the implicit coupled temperature-displacement procedure in ABAQUS/Standard with user subroutines, the corresponding Li concentration and stress-strain fields are updated incrementally. Meanwhile, contour integrations are conducted for the classic Rices J -integral:[38]

$$J_\Gamma = \int_{\Gamma_2} (W_e n_1 - t_i \frac{\partial u_i}{\partial x_1}) d\Gamma \tag{5}$$

where, as shown in Figure 2, t_i is the traction vector on the contour $\partial\Omega$ that around the crack tip, n_i is the unit outward normal on $\partial\Omega$, u_i is the displacement vector, $d\Gamma$ is the length element along the contour, and W_e is the elastic energy density.

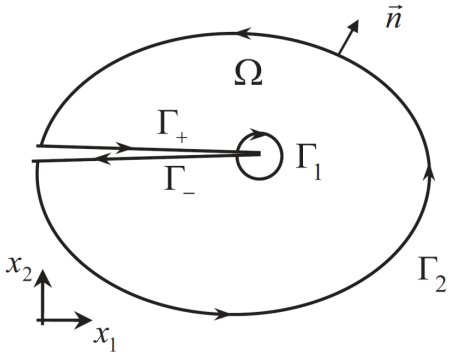

Figure 2. A crack tip contour used in the J-integral calculation. The planar crack is oriented

along the x_1 direction, the region Ω around the crack tip is surrounded by the closed contour $\partial\Omega = \Gamma_1 + \Gamma_- + \Gamma_2 + \Gamma_+$, and $\mathbf{n}$ the unit outward normal on $\partial\Omega$.

3. Results and discussion

Upon successfully setting the simulation cell with corresponding boundary and loading conditions, uniaxial tensile simulations of Li_xSi samples, such as crystalline <111>-Si, *a*-Si, *a*-$Li_{0.25}Si$, *a*-$Li_{0.50}Si$, *a*-$Li_{0.75}Si$, and *a*-$Li_{1.00}Si$, are conducted at 10 K under the strain rate of $5\times10^7\,1/\mathrm{s}$. For the amorphous Li_xSi samples, eight different configurations are simulated for each compositional case to average the obtained results. As shown in Figure 3, the obtained stress-strain curves of *a*-Li_xSi exhibit the typical characteristics of metallic materials.[35] Material properties of pure Si and Li_xSi alloys, such as Young's modulus and yield stress, are estimated from the stress-strain curves. As listed in the Table 1, the Young's modulus and yield stress of Li_xSi alloys are highly dependent on the concentration of Li, while the Poisson's ratio shows much less sensitivity to the variation of Li concentration.

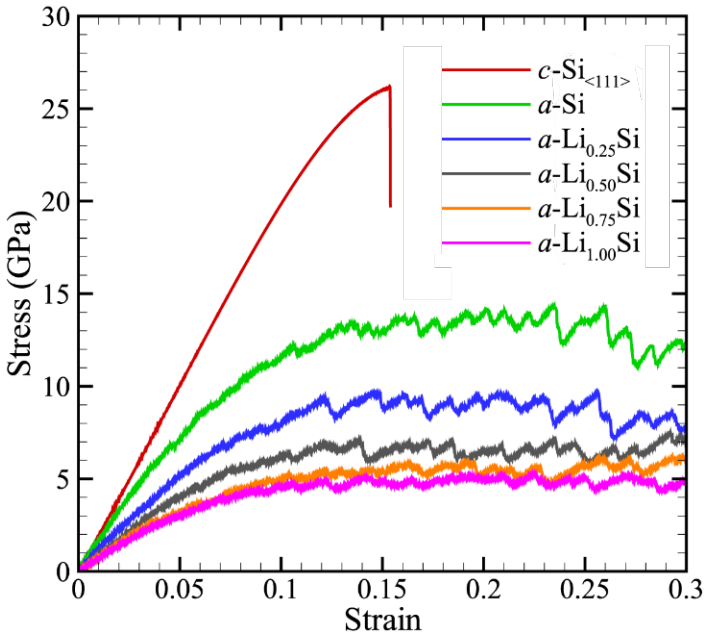

Figure 3. Uniaxial tensile stress-strain curves of crystalline <111>-Si, *a*-Si, and *a*-Li_xSi at 10 K under the strain rate of 5×10^7 1/s .

MD simulations of pre-cracked pure Si and Li_xSi alloy samples are conducted at 10 K to investigate their fracture behavior. During the simulations, interaction between the two pre-exist crack surface is shielded. Under the constant strain rate loading condition, the crack tip open displacement increases gradually. With the increment of Li concentration in the Li_xSi alloy samples, much blunter crack tip can be observed. At the critical moment that the crack starts to propagate, as shown in Figure 1(b) as an example, the critical strain is recorded and listed in Table 2. It should be noted that, as all the MD simulations are conducted with an extremely high strain rate (5×10^7 1/s), the simulation time is too short for Li migration. Therefore, no Li redistribution around crack tip is observed, even though previous studies have already demonstrated that Li atoms are highly mobile and can easily

be driven by stress gradient.[39-45]

Table 1. The Young's modulus (E), Poisson's ratio (ν), and yield stress (σ_Y) of pure Si and Li_xSi alloys obtained from the uniaxial tensile simulations.

	E (GPa)	ν	σ_Y (GPa)
<111>-Si	189.4	0.17	11.7
a-Si	151.7	0.27	6.7
a-$Li_{0.25}Si$	105.6	0.33	5.4
a-$Li_{0.50}Si$	82.8	0.35	4.1
a-$Li_{0.75}Si$	70.8	0.37	2.9
a-$Li_{1.00}Si$	65.9	0.34	2.7

Using the material properties obtained in the above MD simulations as inputs, continuum level chemo-mechanical calculations are conducted for the fracture toughness of pure Si and Li_xSi alloys. The same-size pre-cracked 2D plane strain samples are used, and the corresponding critical strain is applied as the boundary condition. As no Li redistribution is observed in the above MD simulations, Li distribution in the samples is assumed to be uniform throughout the chemo-mechanical simulation. Therefore, for simplicity of the model, no Li transport needs to be considered in the chemo-mechanical modeling. As a demonstration of the method presented in this study, we first calculated the fracture toughness of <111>-Si as $J_C = 3.60\ \mathrm{J/m^2}$ based on the contour integration of the classic Rices J-integral, leading to the critical stress intensity factor as

$K_{\mathrm{IC}<111>} = \sqrt{J_{\mathrm{C}} \frac{E}{1-\nu^2}} = 0.84$ MPa$\sqrt{\mathrm{m}}$, which is in a good agreement with the reported experimental measurements, namely K_{IC}=0.83~0.95MPa$\cdot\sqrt{\mathrm{m}}$.[46-47] This calculation indicates that the approach presented here is appropriate for the derivation of fracture toughness. With confidence in the method, we next calculated the fracture toughness (J_{C}) of *a*-Si and Li_xSi alloys, as listed in Table 2. The obtained J_{C} for the low Li concentration cases investigated in this study matches the experimental results published by Pharr *et al* reasonably well.[22] In addition, with the increment of Li concentration in the Li_xSi alloys, the J_{C} decreases first to a minimum value around $Li_{0.25}Si$ and then increases. This trend also agrees with the previous experimental measurement conducted by Wang *et al*.[23]

It should be noted that, as high strain rate is used in the above study, Li transport during the chemo-mechanical calculation of fracture toughness can be neglected. However, in reality, the loading time scale in quasi-static fracture toughness measurements is comparable to the Li diffusion time scale.[43] Therefore, it is important to consider the Li redistribution caused by the stress gradient around the crack tip.[45]

Table 2. The critical strain and fracture toughness (J_{C}) of pure Si and Li_xSi alloys obtained from MD simulation and chemo-mechanical modeling, respectively.

	Critical strain	J_{C} (J/m^2)
<111>-Si	0.0245	3.60
a-Si	0.0341	5.80

a-$Li_{0.25}Si$	0.0363	4.73
a-$Li_{0.50}Si$	0.0441	5.39
a-$Li_{0.75}Si$	0.0449	5.29
a-$Li_{1.00}Si$	0.0450	4.80

As shown in Figure 4, when a cracked specimen with width $L_0 = 500$ Å, initial crack length $a_0 = 90$ Å, and initial Li concentration c_0 is loaded with a far field stress σ_0 which is much less than the yield stress σ_Y along the vertical direction, the normalized effective stress σ_{eff} / σ_Y is shown in Figure 4(a). Without considering Li transport, the initial uniform Li distribution is unaltered in the sample, therefore the normalized changed amount of Li concentration due to the far field loading is $\Delta c / c_0 = 0$ (Figure 4(b)), and the normalized classic Rices J -integral (Figure 4(c)) obtained from three different integration contours (as shown in Fig. S1 in the Supporting Information) are overlapping with each other, indicating that the J-integral is path-independent. However, if stress gradient driving Li transportation effect is considered and the Li diffusion constant is set to be $D = 1 \times 10^{-14} \frac{m^2}{s}$,[43] with the same far field stress loading condition, the crack tip stress gradient can drive Li to aggregate around the crack tip (Figure 4(e)), causing more severe stress concentration at the crack tip (Figure 4(d)). In addition, Li concentration gradient around the crack tip can lead to the path-dependent behavior of the classic Rices J -integral, as shown in Figure 4(f).

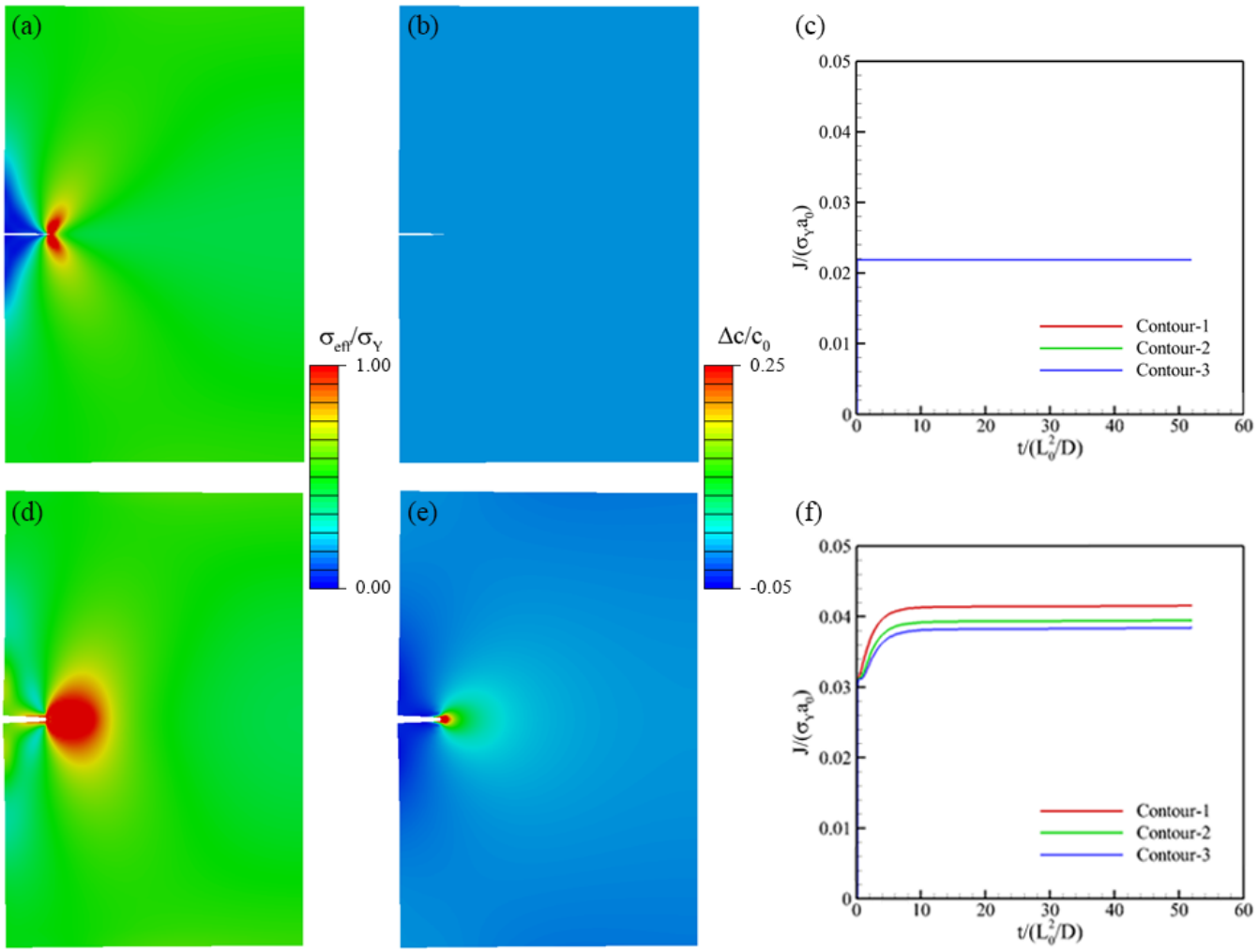

Figure 4. Compared with the normalized effective stress (a), normalized changed amount of Li concentration (b), and normalized classic Rice's J-integral (c) obtained from the case without Li transport, under the same far field stress loading conditions, the crack tip stress gradient can drive Li to aggregate around the crack tip (e), causing more severe stress concentration at the crack tip (d), and leading to the path-dependent behavior of the classic Rices J -integral (f).

In order to overcome the limitation of the classic Rices J -integral when there exists

a Li concentration gradient, the newly developed chemo-mechanical J-integral needs to be used for the estimation of fracture toughness.[37, 48] The chemo-mechanical J-integral is defined by:

$$J_{\Gamma}^{cm} = \int_{\Gamma_2} (\psi n_1 - t_i \frac{\partial u_i}{\partial x_1}) d\Gamma \,, \quad \psi = W_e - (\mu - \mu_0)c - TS \,, \tag{6}$$

where, ψ is the grand potential of the system, T is the absolute temperature, and S is the entropy of mixing per volume of mixture giving by:

$$S = -R_g c_{\max} \left[\frac{c}{c_{\max}} \log(\frac{c}{c_{\max}}) + (1 - \frac{c}{c_{\max}}) \log(1 - \frac{c}{c_{\max}}) \right] . \tag{7}$$

Using this chemo-mechanical J-integral, the crack driving forces for the case with Li transport are calculated, as shown in Figure 5. It should be noted that, as the contribution of Li is considered in the grand potential term in Eq. (6), the calculated chemo-mechanical J-integral is normalized by $(\sigma_Y + R_g \mathrm{T} c_{\max}) \cdot \mathrm{a}_0$ rather than $\sigma_Y \cdot \mathrm{a}_0$ that the classic Rices J-integral is normalized by. With the Li flow caused by crack tip stress gradient, the chemo-mechanical J-integrals obtained from different integration contours differ slightly from each other. Once the Li redistribution reaches a steady state, the chemo-mechanical J-integrals will finally converge to a single value, indicating the path-independent property of the chemo-mechanical J-integral.

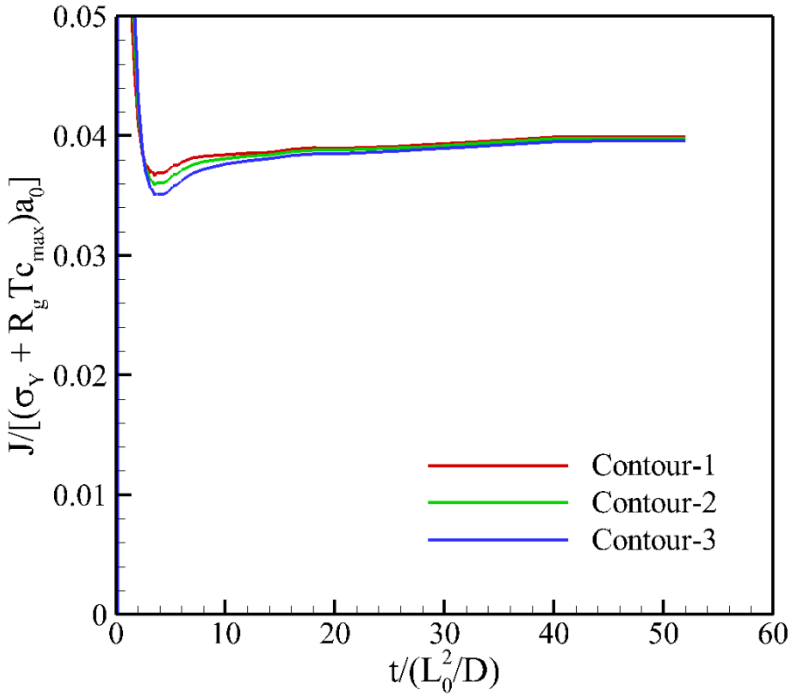

Figure 5. Normalized chemo-mechanical J-integrals obtained from different integration contours. With the Li flow caused by crack tip stress gradient, the chemo-mechanical J-integrals obtained from different integration contours differ slightly from each other. Once the Li redistribution reaches a steady state, the chemo-mechanical J-integrals will finally converge to a single value, indicating the path-independent property of the chemo-mechanical J-integral.

4. Conclusions

In conclusion, we have presented a molecular dynamics (MD) simulation informed continuum chemo-mechanical model with conservation integrals for the investigation of fracture toughness of Li_xSi alloys. In this model, MD simulations are used to calculate the material properties and the critical fracture strain of Li_xSi alloys. Using the obtained MD

simulation results as inputs, continuum level chemo-mechanical simulations are conducted for the stress field and thus the fracture toughness of Li_xSi samples with small scale yielding.

Using the presented model, we investigated the fracture toughness (J_C) of Li_xSi alloys with low Li concentration. Our modeling results, which are reasonably consistent with the limited published results derived from different experimental measurements, revealed that the fracture toughness of Li_xSi alloys with low Li concentration does not vary significantly with Li concentration. In addition, we demonstrated that, when the loading time scale of fracture test is comparable to the Li diffusion time scale, Li redistribution caused by the stress gradient around crack tip needs to be considered, as stress gradient can drive Li to migrate from the far field to crack tip, leading to the aggregation of Li there, and this process is both thermodynamically and kinetically favorable. Under such circumstance, the classic Rices J-integral becomes path-dependent. Therefore, an appropriate chemo-mechanical path-independent J-integral needs to be used for the estimation of fracture toughness. The obtained fracture toughness of the Li_xSi alloys here provides guidance for the rational design of Si based electrodes, and the approach presented in this study also sheds light for the evaluation of the fracture toughness of other energy materials at different charging/discharging levels.

Acknowledgements:

H.Y. acknowledges the National 1000 Talents Program of China tenable at the Huazhong University of Science and Technology (HUST), China. H.Y. and J.M.Q. acknowledge

National Science Foundation support under grants CMMI-1624313.

ORCID:

Hui Yang: 0000-0002-2628-4676

Conflict of Interest:

The authors declare no competing financial interest.

References:

(1) Tarascon, J. M. Key challenges in future Li-battery research. *Philos. Trans. R. Soc. A-Math. Phys. Eng. Sci.* **2010,** *368*, 3227-3241.
(2) Tarascon, J. M.; Armand, M. Issues and challenges facing rechargeable lithium batteries. *Nature* **2001,** *414*, 359-367.
(3) Chu, S.; Cui, Y.; Liu, N. The path towards sustainable energy. *Nature Materials* **2016,** *16*, 16.
(4) Li, M.; Lu, J.; Chen, Z.; Amine, K. 30 Years of Lithium‐Ion Batteries. *Advanced Materials* **2018,** *30*, 1800561.
(5) Marom, R.; Amalraj, S. F.; Leifer, N.; Jacob, D.; Aurbach, D. A review of advanced and practical lithium battery materials. *J. Mater. Chem.* **2011,** *21*, 9938-9954.
(6) Takada, K. Progress and prospective of solid-state lithium batteries. *Acta Materialia* **2013,** *61*, 759-770.
(7) Lu, J.; Chen, Z.; Pan, F.; Cui, Y.; Amine, K. High-Performance Anode Materials for Rechargeable Lithium-Ion Batteries. *Electrochemical Energy Reviews* **2018,** *1*, 35-53.
(8) Zuo, X.; Zhu, J.; Müller-Buschbaum, P.; Cheng, Y.-J. Silicon based lithium-ion battery anodes: A chronicle perspective review. *Nano Energy* **2017,** *31*, 113-143.
(9) Zhang, W. J. A review of the electrochemical performance of alloy anodes for lithium-ion batteries. *J. Power Sources* **2011,** *196*, 13-24.
(10) Kamali, A. R.; Fray, D. J. Review on Carbon and Silicon Based Materials as Anode Materials for Lithium Ion Batteries. *J. New Mat.Electrochem. Syst.* **2010,** *13*, 147-160.
(11) Liu, X. H.; Zheng, H.; Zhong, L.; Huang, S.; Karki, K.; Zhang, L. Q.; Liu, Y.;

Kushima, A.; Liang, W. T.; Wang, J. W.; Cho, J.-H.; Epstein, E.; Dayeh, S. A.; Picraux, S. T.; Zhu, T.; Li, J.; Sullivan, J. P.; Cumings, J.; Wang, C.; Mao, S. X.; Ye, Z. Z.; Zhang, S.; Huang, J. Y. Anisotropic Swelling and Fracture of Silicon Nanowires during Lithiation. *Nano Letters* **2011,** *11*, 3312-3318.
(12) McDowell, M. T.; Ryu, I.; Lee, S. W.; Wang, C.; Nix, W. D.; Cui, Y. Studying the Kinetics of Crystalline Silicon Nanoparticle Lithiation with In Situ Transmission Electron Microscopy. *Advanced Materials* **2012,** *24*, 6034-6041.
(13) Zhao, K.; Cui, Y. Understanding the role of mechanics in energy materials: A perspective. *Extreme Mechanics Letters* **2016,** *9*, 347-352.
(14) Lee, S. W.; McDowell, M. T.; Berla, L. A.; Nix, W. D.; Cui, Y. Fracture of crystalline silicon nanopillars during electrochemical lithium insertion. *Proc. Natl. Acad. Sci. U. S. A.* **2012,** *109*, 4080-4085.
(15) Liu, X. H.; Zhong, L.; Huang, S.; Mao, S. X.; Zhu, T.; Huang, J. Y. Size-Dependent Fracture of Silicon Nanoparticles During Lithiation. *Acs Nano* **2012,** *6*, 1522-1531.
(16) Liang, W.; Yang, H.; Fan, F.; Liu, Y.; Liu, X. H.; Huang, J. Y.; Zhu, T.; Zhang, S. Tough Germanium Nanoparticles under Electrochemical Cycling. *Acs Nano* **2013,** *7*, 3427-3433.
(17) Yang, H.; Huang, S.; Huang, X.; Fan, F.; Liang, W.; Liu, X. H.; Chen, L.-Q.; Huang, J. Y.; Li, J.; Zhu, T.; Zhang, S. Orientation-Dependent Interfacial Mobility Governs the Anisotropic Swelling in Lithiated Silicon Nanowires. *Nano Letters* **2012,** *12*, 1953-1958.
(18) Yang, H.; Liang, W.; Guo, X.; Wang, C.-M.; Zhang, S. Strong kinetics-stress coupling in lithiation of Si and Ge anodes. *Extreme Mechanics Letters* **2015,** *2*, 1-6.
(19) Lee, S. W.; Ryu, I.; Nix, W. D.; Cui, Y. Fracture of crystalline germanium during electrochemical lithium insertion. *Extreme Mechanics Letters* **2015,** *2*, 15-19.
(20) McDowell, M. T.; Lee, S. W.; Harris, J. T.; Korgel, B. A.; Wang, C.; Nix, W. D.; Cui, Y. In Situ TEM of Two-Phase Lithiation of Amorphous Silicon Nanospheres. *Nano Letters* **2013,** *13*, 758-764.
(21) Wang, J. W.; He, Y.; Fan, F.; Liu, X. H.; Xia, S.; Liu, Y.; Harris, C. T.; Li, H.; Huang, J. Y.; Mao, S. X.; Zhu, T. Two-Phase Electrochemical Lithiation in Amorphous Silicon. *Nano Letters* **2013,** *13*, 709-715.
(22) Pharr, M.; Suo, Z.; Vlassak, J. J. Measurements of the Fracture Energy of Lithiated Silicon Electrodes of Li-Ion Batteries. *Nano Letters* **2013,** *13*, 5570-5577.
(23) Wang, X.; Fan, F.; Wang, J.; Wang, H.; Tao, S.; Yang, A.; Liu, Y.; Beng Chew, H.; Mao, S. X.; Zhu, T.; Xia, S. High damage tolerance of electrochemically lithiated silicon. *Nat Commun* **2015,** *6*.
(24) Swadener, J. G.; Baskes, M. I.; Nastasi, M. Molecular Dynamics Simulation of Brittle Fracture in Silicon. *Physical Review Letters* **2002,** *89*, 085503.
(25) Hauch, J. A.; Holland, D.; Marder, M. P.; Swinney, H. L. Dynamic Fracture in Single Crystal Silicon. *Physical Review Letters* **1999,** *82*, 3823-3826.

(26) Holland, D.; Marder, M. Ideal Brittle Fracture of Silicon Studied with Molecular Dynamics. *Physical Review Letters* **1998,** *80*, 746-749.
(27) Farkas, D.; Van Swygenhoven, H.; Derlet, P. M. Intergranular fracture in nanocrystalline metals. *Physical Review B* **2002,** *66*, 060101.
(28) Hoagland, R. G.; Daw, M. S.; Foiles, S. M.; Baskes, M. I. An atomic model of crack tip deformation in aluminum using an embedded atom potential. *Journal of Materials Research* **1990,** *5*, 313-324.
(29) Zhao, K.; Pharr, M.; Cai, S.; Vlassak, J. J.; Suo, Z. Large Plastic Deformation in High-Capacity Lithium-Ion Batteries Caused by Charge and Discharge. *Journal of the American Ceramic Society* **2011,** *94*, s226-s235.
(30) Zhao, K.; Wang, W. L.; Gregoire, J.; Pharr, M.; Suo, Z.; Vlassak, J. J.; Kaxiras, E. Lithium-Assisted Plastic Deformation of Silicon Electrodes in Lithium-Ion Batteries: A First-Principles Theoretical Study. *Nano Letters* **2011,** *11*, 2962-2967.
(31) Cui, Z.; Gao, F.; Qu, J. A finite deformation stress-dependent chemical potential and its applications to lithium ion batteries. *Journal of the Mechanics and Physics of Solids* **2012,** *60*, 1280-1295.
(32) Yang, H.; Fan, F.; Liang, W.; Guo, X.; Zhu, T.; Zhang, S. A chemo-mechanical model of lithiation in silicon. *Journal of the Mechanics and Physics of Solids* **2014,** *70*, 349-361.
(33) Cui, Z.; Gao, F.; Cui, Z.; Qu, J. A second nearest-neighbor embedded atom method interatomic potential for Li–Si alloys. *J. Power Sources* **2012,** *207*, 150-159.
(34) Cui, Z.; Gao, F.; Cui, Z.; Qu, J. Developing a second nearest-neighbor modified embedded atom method interatomic potential for lithium. *Modelling and Simulation in Materials Science and Engineering* **2012,** *20*, 015014.
(35) Fan, F. F.; Huang, S.; Yang, H.; Raju, M.; Datta, D.; Shenoy, V. B.; van Duin, A. C. T.; Zhang, S. L.; Zhu, T. Mechanical properties of amorphous LixSi alloys: a reactive force field study. *Modelling and Simulation in Materials Science and Engineering* **2013,** *21*, 074002.
(36) Shi, X.; Zhu, J.; Xia, Y.; Fan, F.; Zhang, F.; Gu, M.; Yang, H. Ultrahigh Malleability of the Lithiation-Induced LixSi Phase. *ACS Applied Energy Materials* **2018,** *1*, 4211-4220.
(37) Haftbaradaran, H.; Qu, J. A path-independent integral for fracture of solids under combined electrochemical and mechanical loadings. *Journal of the Mechanics and Physics of Solids* **2014,** *71*, 1-14.
(38) Rice, J. R. A Path Independent Integral and the Approximate Analysis of Strain Concentration by Notches and Cracks. *Journal of Applied Mechanics* **1968,** *35*, 379-386.
(39) Grantab, R.; Shenoy, V. B. Pressure-Gradient Dependent Diffusion and Crack Propagation in Lithiated Silicon Nanowires. *Journal of the Electrochemical Society* **2012,** *159*, A584-A591.
(40) Yang, H.; Huang, X.; Liang, W.; van Duin, A. C. T.; Raju, M.; Zhang, S. Self-weakening in lithiated graphene electrodes. *Chemical Physics Letters* **2013,** *563*, 58-62.

(41) Huang, X.; Yang, H.; Liang, W.; Raju, M.; Terrones, M.; Crespi, V. H.; van Duin, A. C. T.; Zhang, S. Lithiation induced corrosive fracture in defective carbon nanotubes. *Applied Physics Letters* **2013,** *103*, 153901-4.
(42) Gu, M.; Yang, H.; Perea, D. E.; Zhang, J.-G.; Zhang, S.; Wang, C.-M. Bending-Induced Symmetry Breaking of Lithiation in Germanium Nanowires. *Nano Letters* **2014,** *14*, 4622-4627.
(43) Kim, S.; Choi, S. J.; Zhao, K.; Yang, H.; Gobbi, G.; Zhang, S.; Li, J. Electrochemically driven mechanical energy harvesting. *Nat Commun* **2016,** *7*.
(44) Chen, T.; Yang, H.; Li, J.; Zhang, S. Mechanics of electrochemically driven mechanical energy harvesting. *Extreme Mechanics Letters* **2017,** *15*, 78-82.
(45) Yang, L.; Chen, H.-S.; Jiang, H.; Song, W.-L.; Fang, D. Lithium redistribution around the crack tip of lithium-ion battery electrodes. *Scripta Materialia* **2019,** *167*, 11-15.
(46) Ericson, F.; Johansson, S.; Schweitz, J.-Å. Hardness and fracture toughness of semiconducting materials studied by indentation and erosion techniques. *Materials Science and Engineering: A* **1988,** *105*, 131-141.
(47) Masolin, A.; Bouchard, P.-O.; Martini, R.; Bernacki, M. Thermo-mechanical and fracture properties in single-crystal silicon. *Journal of Materials Science* **2013,** *48*, 979-988.
(48) Gao, Y. F.; Zhou, M. Coupled mechano-diffusional driving forces for fracture in electrode materials. *J. Power Sources* **2013,** *230*, 176-193.